

# Effects of Coating Characteristics of One-Step Aerosol Synthesized–Silica-Coated FeNi Nanostructured Particles on Powder Core Properties for Electronic Machines Development

*Eka Lutfi Septiani <sup>a</sup>, Nobuhiro Okuda <sup>b</sup>, Hiroyuki Matsumoto <sup>b</sup>, Kiet Le Anh Cao <sup>a</sup>,  
Tomoyuki Hirano <sup>a</sup>, and Takashi Ogi <sup>a \*</sup>*

<sup>a</sup>Chemical Engineering Program, Department of Advanced Science and Engineering, Graduate  
School of Advanced Science and Engineering, Hiroshima University, 1-4-1 Kagamiyama,  
Higashi-Hiroshima, Hiroshima 739-8527, Japan

<sup>b</sup>Materials Research Center, Technology & Intellectual Property HQ, TDK corporation,  
570-2 Matsugashita, Minami-Hadori, Narita, Chiba 286-8588, Japan

\*Corresponding author: Takashi Ogi, [ogit@hiroshima-u.ac.jp](mailto:ogit@hiroshima-u.ac.jp)

Tel/Fax: +81-82-424-3765

## Abstract

Nanostructured particles with a core-shell structure have been highlighted in recent developments in various fields, including electronic machinery applications. Applying nonagglomerated nano scaled-silica-coated soft-magnetic particles into powder core inductors (PCIs), a power converter in the electronic machines, promises its efficiency improvement. In this study, nanostructuring silica-coated FeNi (FeNi@SiO<sub>2</sub>) particles was conducted via aerosol method by introducing the SiO<sub>2</sub> (0.4 nm) from hexamethyldisiloxane to the FeNi particles. The effect of varying the supplied amounts of FeNi (as the core) and SiO<sub>2</sub> (as the shell) materials on the core-shell structure and electrical properties of a powder core was investigated. The results revealed that controlling the FeNi core number ( $N_{\text{FeNi}}$ ) played a critical role in determining the coating characteristics. Applying a higher  $N_{\text{FeNi}}$  yielded superior coating properties, characterized by decreased shell inhomogeneity and pristine silica nanoparticles due to heterogeneous nucleation. Notably, a higher level of shell inhomogeneity and the presence of silica nanoparticles caused increased eddy current loss and decreased breakdown voltage in the powder core. This is the first study to elucidate the correlation between the structure of FeNi@SiO<sub>2</sub> particles and the electrical properties of a powder core. This study provides insights into the factors influencing nano scaled-coating characteristics and powder core properties, which are crucial for advancing the electronic components.

Keywords: shell inhomogeneity, core-shell nanostructure, soft magnetic, eddy current loss, breakdown voltage

## 1. Introduction

Nanostructured materials have revolutionized diverse fields like energy, food, and environment due to their exceptional versatility.<sup>1-6</sup> Their unique properties arise from their intricate morphologies, which can vary widely including porous, hollow, dense, core-shell, and so forth. In recent years, the rapid advancement of technology has spurred the development of electric devices demanding innovative solutions to increase efficiency and compact their designs.<sup>7</sup> In this context, nanostructured materials has garnered significant attention and intention, controlling the owing to its potential to address the evolving needs of modern electronics effectively. The evolution of high-current and -frequency operating systems in devices and machines is a critical aspect driving this progress. The primary requirement of these systems is a power converter component.<sup>8</sup> Powder core inductors (PCIs), comprising densely soft magnetic powder cores and winding coils, are highly suitable power converters owing to their adaptability to high current applications.<sup>9</sup> Nanostructuring soft-magnetic particles from hollow to dense improves the DC bias property of the PCIs.<sup>10</sup> However, the optimal performance of powder cores also relies on several key properties, including low eddy current loss and high breakdown voltage. When the eddy current loss is high, the power waste as heat becomes high, leading to a temperature rise in the core material.<sup>11</sup> A lower eddy current loss indicates that a greater portion of electrical energy is effectively converted into magnetic energy, and vice versa. Meanwhile, a higher breakdown voltage is essential for the insulation reliability and safety of the PCI and overall electronic system.<sup>12</sup> Therefore, the application of the core-shell nanostructured soft magnetic particles is necessary to achieve these properties. The insulation layer from the shell creates a barrier between individual soft magnetic particles that allows less energy dissipation within the core and enhances dielectric strength to withstand electric stress without breaking down.<sup>13</sup>

Silica-coated FeNi (FeNi@SiO<sub>2</sub>) particles emerge as nanostructured materials with significant promise for advancing magnetic components. In this case, the FeNi@SiO<sub>2</sub> particles with a core-shell structure leverages the unique properties of high saturated magnetization and permeability from the FeNi core and high stability from the silica shell.<sup>14–17</sup> Moreover, the magnetic characteristic of the FeNi core is essential in maintaining the minimum size of a PCI (see Equation 1 for explanation).<sup>18</sup>

$$L = \frac{\mu AN^2}{l} \quad (1)$$

where  $L$  is the inductance (H), associated with the inductor's ability to store magnetic energy, and  $\mu$  is the permeability (Wb/A.m), contributed by the powder core materials.  $N$  is the number of turns in the coil,  $A$  is the effective cross-sectional area of the core (m<sup>2</sup>), and  $l$  is the effective magnetic path length in the core (m). Thus, in PCI miniaturization, designing materials with high  $\mu$  is crucial to achieving low  $A$ ,  $l$ , and  $N$ . Furthermore, FeNi@SiO<sub>2</sub> particle morphology and SiO<sub>2</sub> shell coating characteristics, including shell thickness, shell inhomogeneity, and presence of impurities resulting from the coating process, are believed to influence the powder core properties. Dense structured, smooth surfaced and spherical shaped particles are desired to improve the powder core packing density, which results in a stable PCI under a high current load.<sup>10,19</sup> In addition, a high shell thickness, low shell inhomogeneity, and low impurity may guarantee the insulation reliability of PCI in high-frequency applications.<sup>20</sup>

Nanostructuring silica-based core-shell particles via gas phase method has shown the most notable among recent methods, offering a one-step process, hermetically sealed coating, smooth shell, and single core-shell particles.<sup>21–29</sup> This method adapts the chemical vapor deposition technique, in which the seed particle as the core material and the silica source vapor as the shell material are transported in the reactor.<sup>30–32</sup> The silica monomers, nuclei, clusters, and nanoparticles

are generated and deposited on the core material to form a silica shell during the synthesis process. Some researchers have conducted silica-coated particle synthesis using a tubular reactor equipped with a hot wall furnace,<sup>21,22</sup> photoinduction,<sup>31,33,34</sup> plasma and microwave radiation,<sup>35,36</sup> electron beam evaporation,<sup>37</sup> and flame combustion.<sup>21,38–40</sup> These methods yielded particles ranging from nanometer to submicron sizes. Inspired by these works, our group has developed a facile nanostructuring method using a tubular reactor surrounded by a hot wall reactor in a closed system, termed swirler connector-assisted spray pyrolysis (SCA-SP).<sup>15,41</sup> This system provides a reduction atmosphere and uniform mixing between the FeNi core particle and the SiO<sub>2</sub> shell material to successfully yield FeNi@SiO<sub>2</sub> particles.<sup>27,28,42–44</sup> However, the resulted average shell thickness in our previous studies and the aforementioned methods was in a narrow range below 50 nm. Moreover, the effect of coating characteristics on powder core electrical properties remains unexplored. While a thicker shell in nanometer range is expected to improve the powder core characteristics for high voltage applications,<sup>45</sup> shell homogeneity and impurity are some factors that may affect these applications. To clarify this issue, FeNi@SiO<sub>2</sub> particles with various nanoscale shell thicknesses (below 100 nm) and different shell inhomogeneities and impurity levels were investigated. Thus, another approach in the synthesizing process is needed to address this requirement.

In the current study, the effect of the supplied core material ( $N_{\text{FeNi}}$ , the number of FeNi core particles per total dry gas) on the coating characteristics of nanostructured FeNi@SiO<sub>2</sub> particle was examined. The control of  $N_{\text{FeNi}}$  in the SCA-SP method may affect the distribution of FeNi and silica aerosol in the system, which determines the shell thickness and coating characteristics at nanoscale level. Investigating this parameter is crucial for comprehending the impact of shell thickness in nanometer scale across a wide range and the coating characteristics on powder core

properties, especially core loss and breakdown voltage. To gain deeper insights into the significance of the  $N_{\text{FeNi}}$  effect in synthesizing FeNi@SiO<sub>2</sub> particles, the impact of varying the supplied silica was examined. This involved examining the ratio of the supplied SiO<sub>2</sub> ( $N_{\text{SiO}_2}$ , number of SiO<sub>2</sub> monomer per total dry gas) to the  $N_{\text{FeNi}}$ . Through systematic experimentation and analysis, this study provides valuable insights that can inform the process design of nanostructuring material and optimization of the nanoscale shell of the particles for powder cores to realize sustainability.

## 2. Experimental section

### 2.1. Synthesis of FeNi@SiO<sub>2</sub> particles

A typical metal salt solution, with a concentration of 0.2 mol/L, containing Fe(NO<sub>3</sub>)<sub>3</sub>·9H<sub>2</sub>O and Ni(NO<sub>3</sub>)<sub>2</sub>·6H<sub>2</sub>O (FUJIFILM Wako Pure Chemical Corporation, Osaka, Japan) was prepared using a mixture of ultrapure water and 25 vol% ethanol as the solvent. This solution served as the FeNi precursor. Ethanol (Japan Alcohol Corporation, Tokyo, Japan) in the solvent was used to supply reduction gases (i.e., H<sub>2</sub> and CO) to obtain FeNi particles. Hexamethyldisiloxane (HMDSO), which was kept in a bubbler at a temperature of 8°C ( $T_s$ ), was prepared as a silica precursor. A mixture of 5%H<sub>2</sub>–Ar gas was used to carry the FeNi and silica precursors within the synthesis system. FeNi@SiO<sub>2</sub> particles were fabricated using the SCA-SP method (see **Figure 1**). This method comprises an ultrasonic nebulizer; a preheater made of quartz glass with a 395 mm length and 36 mm diameter; a connector with 20 mm length, 20 mm diameter, and 3 mm diameter tangential inlet; and a spray pyrolysis reactor with five tunable heating furnaces with 1,300 mm length and 30 mm diameter.

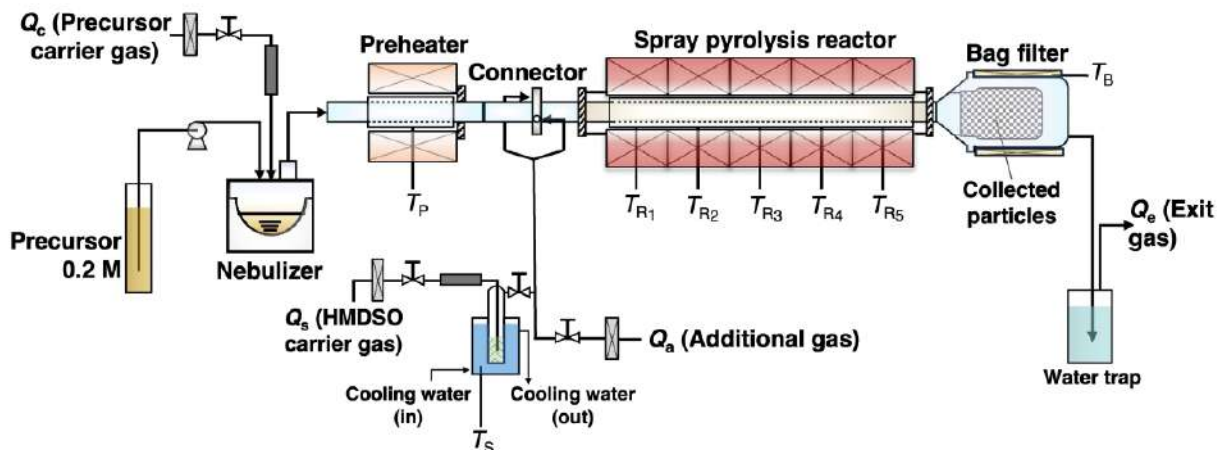


**Figure 1.** Experimental setup of swirl-connector-assisted spray pyrolysis (SCA-SP) for synthesizing FeNi@SiO<sub>2</sub> particles.

First, the FeNi precursor solution was atomized to form droplets through an ultrasonic nebulizer. In this study, the atomized solution was adjusted to 0.8 and 1 mL/s to supply different numbers of FeNi precursor droplets ( $N_{\text{FeNi}}$ ) at  $1.9 \times 10^6$  and  $2.5 \times 10^6$  droplets/cm<sup>3</sup> dry gas, respectively. Supporting Information and **Figure S1** present the detailed experimental setup for the empirical calculation of the number of FeNi precursor droplets ( $N_{\text{FeNi}}$ ). The droplets were transported by 5% H<sub>2</sub>–Ar of carrier gas ( $Q_c$ ) at a flow rate of 5 L/min into the preheater kept at 900°C ( $T_p$ ). The FeNi precursor droplets were decomposed and altered into solid particles comprising iron–nickel–oxide (FeNiO).<sup>41</sup> Second, the generated FeNiO solid particles from the preheater were introduced by the silica precursor in the connector. The silica precursor was carried by 5% H<sub>2</sub>–Ar gas with controlled flow rates ( $Q_s$ ) ranging from 5 to 30 mL/min, providing the amount of supplied silica from 0.033 to 0.198 g/h (detail calculation is described in Supporting Information). To maintain the silica precursor distribution in the system, an additional gas containing 5% H<sub>2</sub>–Ar gas ( $Q_a$ ) was added at 3 L/min. This  $Q_a$  resulted in a relatively high tangential

inlet velocity in the connector, leading to a swirling flow for adequate mixing in the system. Third, the mixture of FeNiO solid particles and silica precursor from the connector was passed through the spray pyrolysis reactor kept at  $1400^{\circ}\text{C}$  ( $T_{R1}-T_{R5}$ ). In this reactor, the FeNiO solid particles were further reduced by the reduction gases to produce FeNi solid particles simultaneously with the silica coating process. Subsequently, the final product of FeNi@SiO<sub>2</sub> particles was generated and captured by a bag filter kept at  $135^{\circ}\text{C}$  ( $T_B$ ). The primary aspect of this approach lies in its utilization of the swirler connector, which generates a swirling motion within the gas flow comprising FeNi core particles and SiO<sub>2</sub> shell material. This swirling action aids in evenly dispersing both the FeNi core and SiO<sub>2</sub> shell components throughout the reactor. As a result, it initiates a gradual rise in temperature and residence time, along with the gradual decomposition of HMDSO. This process leads the deposition of SiO<sub>2</sub> onto the FeNi particle surfaces through heterogeneous nucleation, rather than the formation of SiO<sub>2</sub> nanoparticles via homogeneous nucleation.<sup>15,41</sup> Furthermore, the effect of the number of FeNi core particles on the coating characteristics, including shell thickness, shell inhomogeneity, and silica nanoparticle generation, was investigated under the following experimental conditions (**Table 1**). The number of FeNi core particles ( $N_{\text{FeNi}}$ ) was assumed to be the same as the number of supplied FeNi precursor droplets, which were  $1.9 \times 10^6$  and  $2.5 \times 10^6$  particle/cm<sup>3</sup> dry gas. Meanwhile, the number of supplied SiO<sub>2</sub> ( $N_{\text{SiO}_2}$ ) was calculated from the theoretical supplied SiO<sub>2</sub> monomers (the detailed information is provided in Supporting Information). The SiO<sub>2</sub> monomer amount was estimated based on the size of two SiO<sub>2</sub> molecules with a diameter of 0.4 nm resulting from the HMDSO reaction. This size is represented as the smallest substance that is possibly formed from HMDSO.<sup>46,47</sup>



## 2.2. Characterization of FeNi@SiO<sub>2</sub> particles

Field emission scanning electron microscopy (FE-SEM; S-5200, 20 kV, Hitachi High-Tech. Corp., Tokyo, Japan) and transmission electron microscopy (TEM; JEM-2010, 200 kV, JEOL Ltd., Tokyo, Japan) were used to observe the morphology and structure of the FeNi@SiO<sub>2</sub> particles, respectively. To confirm the crystal structure of the synthesized particles, X-ray diffraction analysis (XRD; D2 PHASER, Bruker Corp., Billerica, MA, USA) was performed. To understand the effect of shell thickness, the resulting FeNi@SiO<sub>2</sub> particles were combined with micron-sized Fe–Si–B particles in a powder magnetic core at a ratio of 1/4. A B-H analyzer SY-8218 (manufactured by IWATSU ELECTRIC Co., Ltd., Tokyo, Japan) was used to measure core loss—an essential property of a powder magnetic core. To measure this property, primary and secondary windings were applied to the magnetic powder toroidal core, followed by quantification of the excitation current from the alternating current flowing to the primary winding and the electromotive force induced in the secondary winding. The eddy current loss was subsequently determined by analyzing the phase difference between the exciting current and the induced electromotive force. As the phase difference decreases, the loss also decreases. To determine the breakdown voltage, electrodes comprising InGa were initially applied to both the upper and lower surfaces of the cylindrical core. Subsequently, the cylindrical core was placed into an insulation breakdown tester (THK-2011ADMPT, Tamadensoku Co., Ltd., Tokyo, Japan), and the voltage was systematically raised between the electrodes. The point at which the current initiated flow was then recorded as the breakdown voltage.

**Table 1.** Experimental conditions for FeNi@SiO<sub>2</sub> particle synthesis.

Sample <sup>a</sup>	FeNi precursor		Silica precursor		Ratio of $N_{\text{SiO}_2}/N_{\text{FeNi}}$ (SiO <sub>2</sub> monomer/ FeNi particle) $\times 10^{-8}$
	Supplied FeNi precursor (mL/min)	$N_{\text{FeNi}}$ (particle/cm <sup>3</sup> dry gas) $\times 10^{-6}$	HMDSO carrier gas (mL/min)	Supplied SiO <sub>2</sub> (g/h)	
<b>FNS-1.9-29</b>			30	0.198	29
<b>FNS-1.9-19</b>	0.8	1.9	20	0.132	19
<b>FNS-1.9-9.7</b>			10	0.066	9.7
<b>FNS-2.5-23</b>			30	0.198	23
<b>FNS-2.5-15</b>	1.0	2.5	20	0.132	15
<b>FNS-2.5-7.6</b>			10	0.066	7.6
<b>FNS-2.5-3.8</b>			5	0.033	3.8

<sup>a</sup>**FNS-A-B**, where A represents the number of FeNi core particles ( $\times 10^6$  particle/cm<sup>3</sup> dry gas) and B represents the ratio of  $N_{\text{SiO}_2}/N_{\text{FeNi}}$  ( $\times 10^8$  SiO<sub>2</sub> monomer/FeNi particle).

### 3. Results and discussion

#### 3.1. Preparation of FeNi@SiO<sub>2</sub> particles with different numbers of FeNi cores and evaluation of the results on a powder core

In the objective of achieving a thick average shell thickness at nanoscale below 100 nm, the FeNi@SiO<sub>2</sub> particles (i.e., **FNS-1.9-29** and **FNS-2.5-23**) produced with varying numbers of FeNi cores ( $N_{\text{FeNi}}$ ) and the highest  $N_{\text{SiO}_2}/N_{\text{FeNi}}$  ratio were systematically examined. The successful

synthesis of FeNi@SiO<sub>2</sub> particles was initially confirmed through crystal structure analysis using XRD patterns. **Figure 2(a)** depicts identical crystal structures of pure face-centered cubic (fcc) FeNi (JCPDS No. 47–1405) for both samples, with the absence of nickel oxide or iron oxide as comparable to the XRD pattern of synthesized FeNi particle alone. This result not only suggests a complete reduction process but also indicates that the silica coating does not prevent FeNiO reduction into FeNi within the core particles. Moreover, based on the Scherrer equation, the crystal sizes of **FNS-1.9-29** and **FNS-2.5-23** were 51 and 39 nm, respectively. The higher crystal size in the low  $N_{\text{FeNi}}$  (**FNS-1.9-29**) could be attributed to the heat transfer phenomenon. The lower number of FeNi cores resulted in less solvent being evaporated from the droplets, leading to increased heat transfer toward the FeNi core and triggering crystal growth.<sup>10,25,41</sup> Particle morphology analysis revealed spherical and hundreds-nanometer-sized particles with narrowed particle size distribution in both samples (**Figure 2(b)** and **(c)**). However, certain detailed distinctive characteristics were observed. In the low  $N_{\text{FeNi}}$ , the geometric mean diameter of **FNS-1.9-29** was approximately 583 nm ( $\sigma_g$  1.29), with noticeable generated free silica nanoparticles (red arrows). Conversely, in the high  $N_{\text{FeNi}}$ , **FNS-2.5-23** exhibited a smaller geometric mean diameter of approximately 507 nm ( $\sigma_g$  1.36), with hardly noticeable free silica nanoparticles. Compared to the FeNi particles (**Figure S2(a)**), the particles with geometric mean diameter of approximately 422 nm ( $\sigma_g$  1.40) and the absence of free silica nanoparticles, these observations suggest that both samples have been coated with SiO<sub>2</sub>. The generation of free silica nanoparticles in low  $N_{\text{FeNi}}$  indicated an insufficient number of cores to be deposited by a SiO<sub>2</sub> monomer. Moreover, this condition led to a high silica concentration in the mixture components in the system, promoting homogeneous nucleation from the SiO<sub>2</sub> monomer to SiO<sub>2</sub> nanoparticles.<sup>15,41</sup>

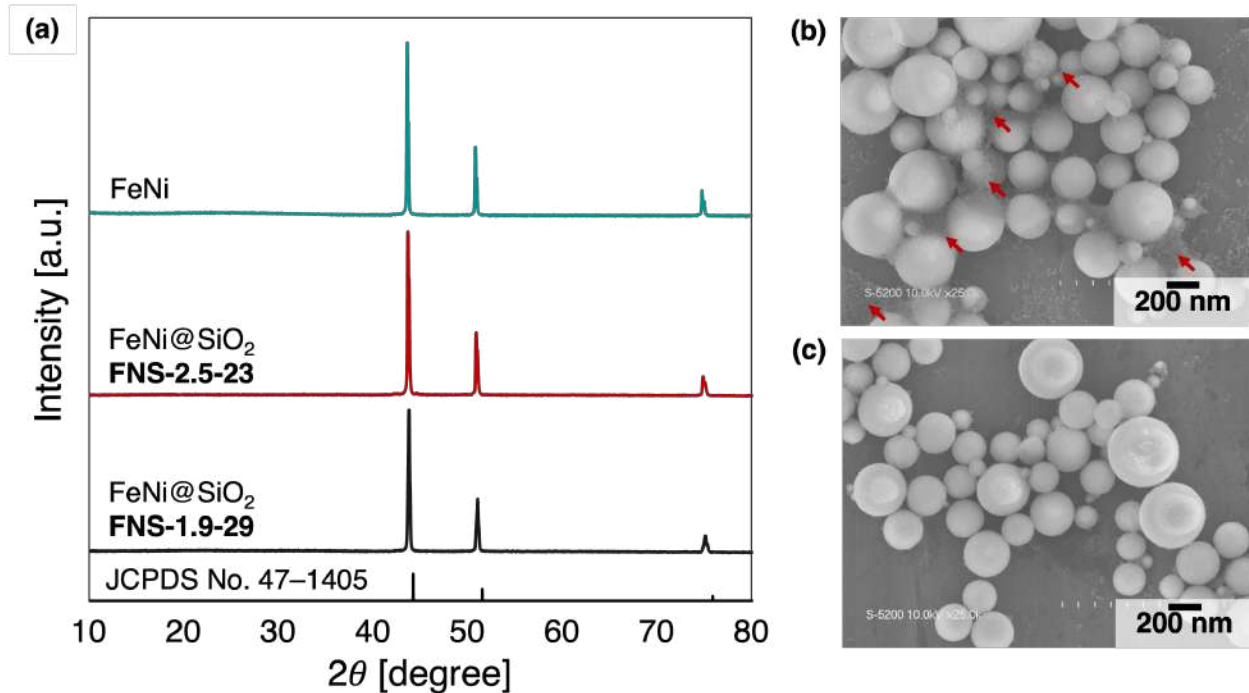


**Figure 2.** (a) XRD pattern and SEM image of the synthesized FeNi and FeNi@SiO<sub>2</sub> particles with different numbers of FeNi core particles, (b) **FNS-1.9-29**, and (c) **FNS-2.5-23**.

The TEM analysis revealed core-shell structured particles in both cases (**Figure 3(a1)** and **(b1)**). It is supported by the TEM image of FeNi particles in **Figure S2 (b)** that indicates a dense particle without any coating layer. In a high magnification TEM image, **Figure 3(a2)** and **(b2)** denote inhomogeneous nanoscale shell thicknesses, indicated by thin ( $t_{s,thin}$ ) and thick ( $t_{s,thick}$ ) shell thicknesses. The average shell thicknesses ( $t_{s,av}$ ) of the particles illustrated in **Figure 3(a3)** and **(b3)** measure approximately 80 and 53 nm in the FeNi@SiO<sub>2</sub> particles for **FNS-1.9-29** and **FNS-2.5-23**, respectively. When the  $N_{FeNi}$  is low, the supplied SiO<sub>2</sub> concentration is relatively high, enabling SiO<sub>2</sub> to scavenge easily on the FeNi particles to form a thicker shell. From these results, the shell inhomogeneity of the particles was qualitatively observed, with the lower  $N_{FeNi}$  ( $1.9 \times 10^6$  particle/cm<sup>3</sup> dry gas) contributing to the higher inhomogeneity due to the insufficient number

of FeNi cores. Moreover, the shell inhomogeneity can be quantified based on the FeNi@SiO<sub>2</sub> particle geometry, including the outer radius ( $R$ ), inner radius ( $r$ ), average shell thickness ( $t_{s,av}$ ), and distance  $d$  moved by core particle ( $\delta$ ) (see **Figure S3**).<sup>48</sup> The shell inhomogeneity,  $(\delta/t_{s,thick}-\delta)$ , was approximately 79% and 53% in **FNS-1.9-29** and **FNS-2.5-23**, respectively.

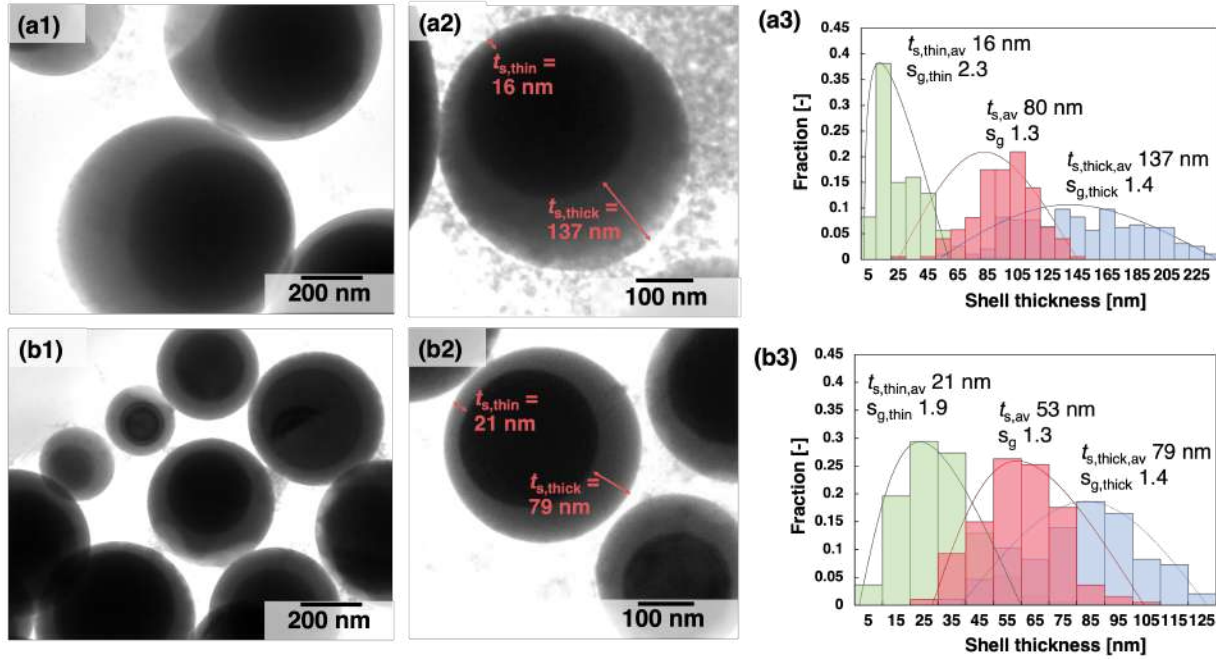


**Figure 3.** TEM images and shell thickness distribution of the synthesized FeNi@SiO<sub>2</sub> particles with different numbers of FeNi core particles: (a) **FNS-1.9-29** and (b) **FNS-2.5-23**. 1) Low magnification and 2) high magnification, indicating shell thickness inhomogeneity; 3) shell thickness distribution.

To evaluate the impact of the core-shell structure on the PCI properties (i.e., eddy current loss and breakdown voltage), the synthesized FeNi@SiO<sub>2</sub> particles were applied as secondary particles to the powder cores. **Figure 4(a)** shows the normalized eddy current loss upon applying both samples. At an equivalent packing density, applying a sample of **FNS-2.5-23** in a powder core resulted in a markedly lower eddy current loss relative to **FNS-1.9-29**. The phenomenon of eddy

current loss within particles, could be elucidated based on Equation (2) which demonstrates its direct correlation with the square of the core particle size as follows<sup>49,50</sup>:

$$P_e = \frac{\eta(\pi B_m D f)^2}{20\rho} \quad (2)$$

Where  $P_e$  is the eddy current loss (W/m<sup>3</sup>),  $\eta$  is the packing density,  $B_m$  is the magnetic flux density (T),  $D$  is the particle size (m),  $f$  is the frequency (Hz),  $\rho$  is the resistivity ( $\Omega$ m). In general, the presence of larger core particles tends to intensify the loss caused by eddy currents. On the other hand, when the size of the core particles decreases, there is usually an increase in the breakdown voltage. This is caused by the greater number of insulating layers between particles per unit volume in the same size of core-shell particle. In this investigation, it is observed that **FNS-2.5-23** exhibit smaller FeNi core particles size, approximately 400 nm, compared to **FNS-2.5-23**, which measure around 440 nm. Therefore, it is plausible to infer that the lower eddy current loss value observed in **FNS-2.5-23** is influenced, to some extent, by their smaller core particle size. Based on the Equation (2), a slight difference in the FeNi core particle diameter (approximately 40 nm) should potentially increase this value by a factor of 1.1<sup>2</sup>. However, this study reveals that the increase in eddy current loss exceeds this theoretical factor. Moreover, despite **FNS-2.5-23** particles exhibiting a lower average shell thickness ( $t_{s,av}$ ), they demonstrate a higher breakdown voltage compared to **FNS-1.9-29** particles (**Figure 4 (b)**). These findings suggest that factors such as shell inhomogeneity and the presence of silica nanoparticles likely play significant roles in determining both eddy current loss and breakdown voltage characteristics. The **FNS-1.9-29** particles (79%) had markedly greater shell inhomogeneity and silica nanoparticle impurity than the **FNS-2.5-23** particles (53%). High shell inhomogeneity potentially signifies exposed FeNi core particle surfaces. This can be inferred from the presence of very thin and very thick shells within the individual particles. The exposed FeNi core and those with very thin shell thicknesses may

have affected the lower electric insulation property, which led to higher eddy current loss and lower breakdown voltage. In addition, the substantial thickness of the shell and the existence of impurities such as free silica nanoparticles—nonconductive materials—may disrupt the uniformity of particle distribution within a powder core, triggering disturbances in electric insulation property. Consequently, the powder core is more prone to electrical breakdown. Meanwhile, when the eddy current loss and breakdown voltage values were the same, the FeNi@SiO<sub>2</sub> particles with  $t_{s,av}$  (53 nm) and shell inhomogeneity (53%) had a higher packing density. Powder core with high packing density is a critical factor in improving the DC bias characteristics of a powder core. To further observed the different coating characteristics of the FeNi@SiO<sub>2</sub> particles, the normalized permeability of the FNS-1.9-29 and FNS-2.5-23 were displayed in Figure S4.

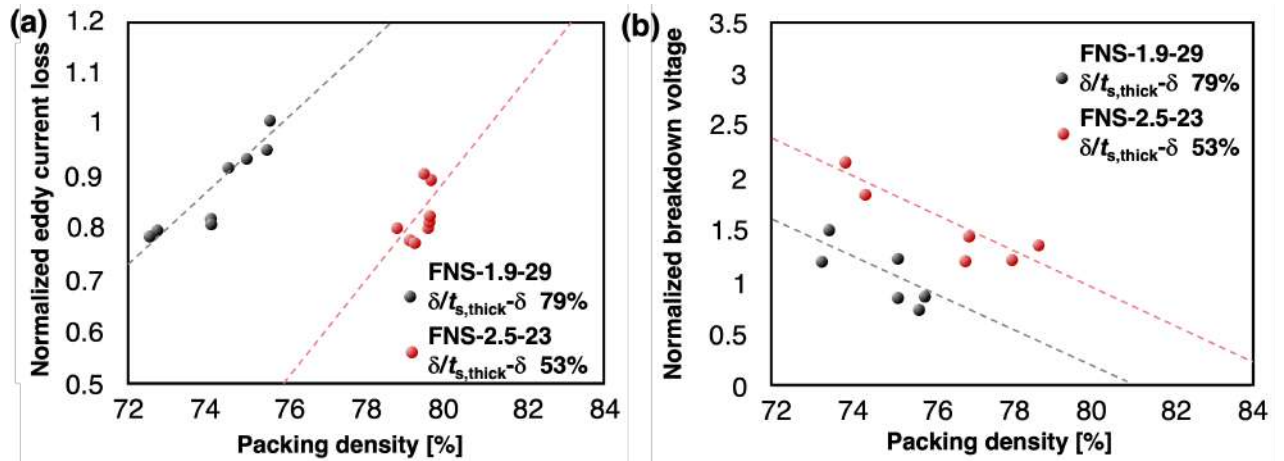


**Figure 4.** (a) Normalized eddy current loss and (b) normalized breakdown voltage at various packing densities of powder cores comprising FeNi@SiO<sub>2</sub> particles from FNS-1.9-29 and FNS-2.5-23 as secondary particles.

### 3.2. Synthesis of FeNi@SiO<sub>2</sub> particles with different numbers of cores and various supplied SiO<sub>2</sub>

To understand the factors that contribute to the particle formation mechanism by applying different numbers of FeNi core ( $N_{\text{FeNi}}$ ), a further investigation was conducted by controlling the ratio of supplied silica to supplied FeNi core ( $N_{\text{SiO}_2}/N_{\text{FeNi}}$ ). As listed in **Table 1**, the  $N_{\text{SiO}_2}/N_{\text{FeNi}}$  ratio was adjusted to  $29 \times 10^8$ ,  $19 \times 10^8$ , and  $9.7 \times 10^8$  SiO<sub>2</sub> monomer/FeNi particles and  $23 \times 10^8$ ,  $15 \times 10^8$ , and  $7.6 \times 10^8$  SiO<sub>2</sub> monomer/FeNi particles in low  $N_{\text{FeNi}}$  ( $1.9 \times 10^6$  particle/cm<sup>3</sup> dry gas) and high  $N_{\text{FeNi}}$  ( $2.5 \times 10^6$  particle/cm<sup>3</sup> dry gas), respectively. All the synthesized particles had a spherical shape, submicron size, and narrow size distribution at any  $N_{\text{SiO}_2}/N_{\text{FeNi}}$  ratio (see the SEM images in **Figure 5**). When the low  $N_{\text{FeNi}}$  was employed, the FeNi@SiO<sub>2</sub> particle diameter ranged from 497 to 583 nm in the  $N_{\text{SiO}_2}/N_{\text{FeNi}}$  ratio range of  $9.7 \times 10^8$ – $29 \times 10^8$  SiO<sub>2</sub> monomer/FeNi particle. Similarly, at high  $N_{\text{FeNi}}$ , the FeNi@SiO<sub>2</sub> particle diameter ranged from 430 to 507 nm in the  $N_{\text{SiO}_2}/N_{\text{FeNi}}$  ratio range of  $7.6 \times 10^8$ – $23 \times 10^8$  SiO<sub>2</sub> monomer/FeNi particle. For the generation of free silica nanoparticles, **Figure 5(a–c)** shows the free silica nanoparticle formation in all samples prepared using low  $N_{\text{FeNi}}$ . A higher  $N_{\text{SiO}_2}/N_{\text{FeNi}}$  ratio, in low  $N_{\text{FeNi}}$ , resulted in a greater number of free silica nanoparticles (red arrows) because of the increased silica concentration in the reactor. In contrast, when a higher  $N_{\text{FeNi}}$  core was applied, the free silica nanoparticles were barely visible in the SEM images at any  $N_{\text{SiO}_2}/N_{\text{FeNi}}$  ratio (see **Figure 5(d–f)**).



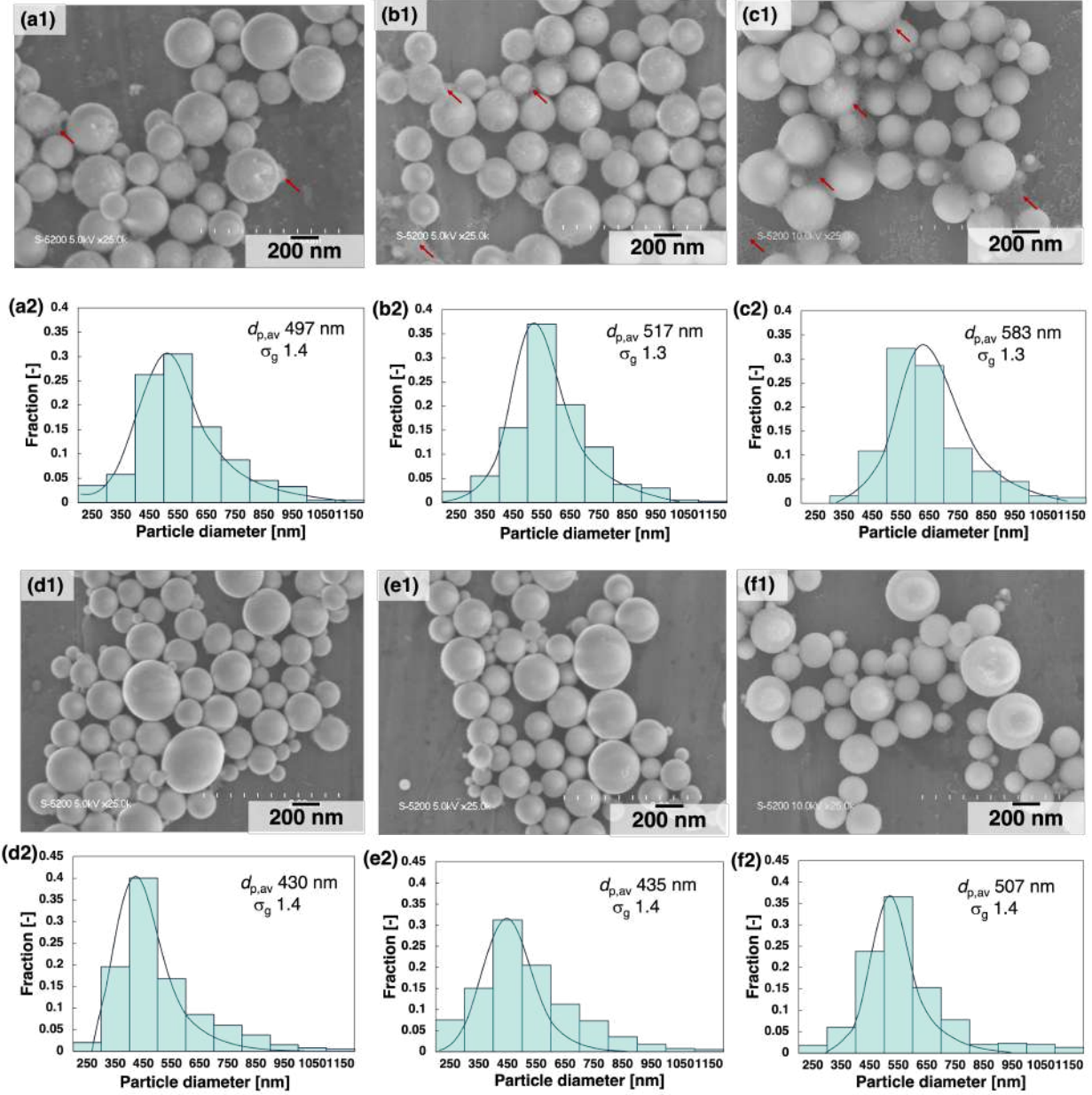


**Figure 5.** Morphology and particle size distribution of the synthesized FeNi@SiO<sub>2</sub> particles with various ratios of silica shell to FeNi core. For low  $N_{\text{FeNi}}$ : (a)  $9.7 \times 10^8$ , (b)  $15 \times 10^8$ , and (c)  $29 \times 10^8$  SiO<sub>2</sub> monomer/FeNi particles. For high  $N_{\text{FeNi}}$ : (d)  $7.6 \times 10^8$ , (e)  $19 \times 10^8$ , and (f)  $29 \times 10^8$  SiO<sub>2</sub> monomer/FeNi particle. 1) SEM image; 2) particle size distribution.

**Figure 6(a1–f1)** further confirms the core–shell structure of the synthesized FeNi@SiO<sub>2</sub> particles in various  $N_{\text{FeNi}}$  and  $N_{\text{SiO}_2}/N_{\text{FeNi}}$ . A notable observation is that the core–shell structure exhibits variations based on the applied  $N_{\text{FeNi}}$ . When low  $N_{\text{FeNi}}$  was utilized, the shell structure exhibited signs of inhomogeneity (asymmetric) across different  $N_{\text{SiO}_2}/N_{\text{FeNi}}$  ratios. The measured percentages of shell inhomogeneity were approximately 73%, 86%, and 79% for **FNS-1.9-9.7**, **FNS-1.9-19**, and **FNS-1.9-29** samples, respectively. Conversely, at high  $N_{\text{FeNi}}$ , the shell tended to display a more homogeneous shell thickness (symmetric), especially at a lower  $N_{\text{SiO}_2}/N_{\text{FeNi}}$  ratio. The percentage of shell inhomogeneity was approximately 29%, 31%, and 53% for **FNS-2.5-7.6**, **FNS-2.5-15**, and **FNS-2.5-23** samples, respectively. To further understand the trend in the high  $N_{\text{FeNi}}$  case, **FNS-2.5-3.8** was synthesized. The characterization of this sample in **Figure S5** shows that the shell inhomogeneity was 27%. This value supported the trend of shell inhomogeneity in this case, in which a lower  $N_{\text{SiO}_2}/N_{\text{FeNi}}$  ratio implied decreased shell inhomogeneity. The distinction of shell inhomogeneity characteristics in both cases can be attributed to differences in the number of FeNi cores available during particle formation. A low  $N_{\text{FeNi}}$  could limit the mixing between SiO<sub>2</sub> and FeNi within the gas flowing in the reactor and the available surface area for SiO<sub>2</sub> deposition, and vice versa. The generation of free silica particles is evidence of this possibility. In terms of varying  $N_{\text{SiO}_2}/N_{\text{FeNi}}$  ratios, **Figure 6(a2–f2)** and **Figure S5** further corroborate that controlling this ratio significantly influences shell thickness. Increasing the  $N_{\text{SiO}_2}/N_{\text{FeNi}}$  ratio from  $9.7 \times 10^8$  to  $29 \times 10^8$  SiO<sub>2</sub> monomer/FeNi particles yielded an increase in the average shell thickness from 27 to 80 nm for low  $N_{\text{FeNi}}$ . Similarly, elevating the  $N_{\text{SiO}_2}/N_{\text{FeNi}}$  ratio from  $3.8 \times 10^8$  to  $23 \times 10^8$  SiO<sub>2</sub> monomer/FeNi particles yielded an improvement in the average shell thickness from 5 to 53 nm for high  $N_{\text{FeNi}}$ . This demonstrates that the shell thickness resulting from silica deposition on the FeNi core is directly related to the high SiO<sub>2</sub> concentration in the aerosol mixture within the reactor.

As seen in the SEM images, the increased availability of the silica precursor resulted in a thicker shell that covered the core, leading to a larger overall particle size.

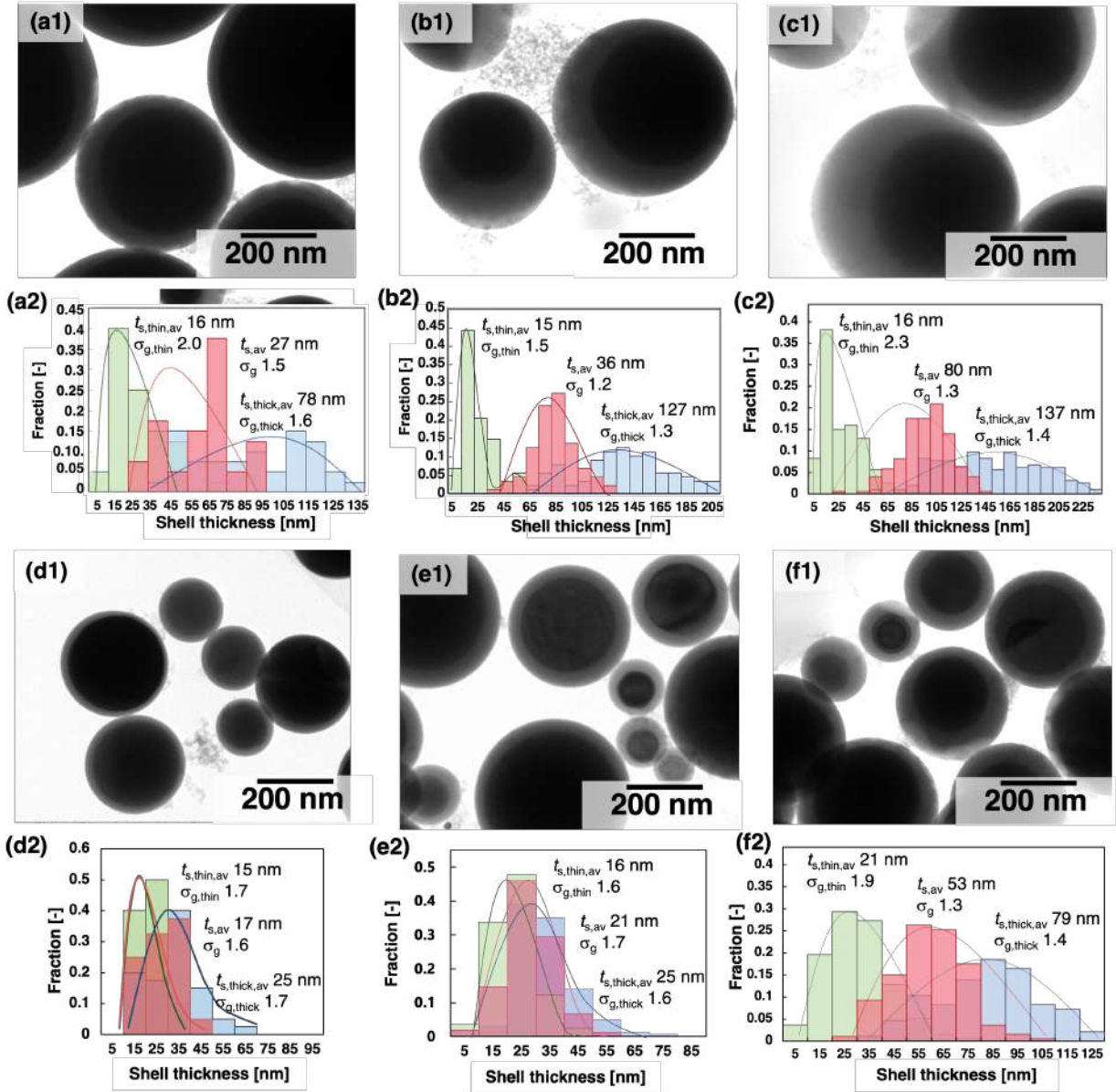


**Figure 6.** Structure and the shell thickness distribution of the synthesized FeNi@SiO<sub>2</sub> particles with various ratios of silica shell to FeNi core. For low  $N_{FeNi}$ : (a)  $42 \times 10^{-3}$ , (b)  $83 \times 10^{-3}$ , (c)  $125 \times 10^{-3}$  SiO<sub>2</sub> monomer/FeNi particle. For high  $N_{FeNi}$ : (d)  $31 \times 10^{-3}$ , (e)  $63 \times 10^{-3}$ , (f)  $94 \times 10^{-3}$  SiO<sub>2</sub> monomer/FeNi particle. 1) TEM image; 2) shell thickness distribution.

Furthermore, regardless of the number of FeNi cores ( $N_{\text{FeNi}}$ ), the correlation between the  $N_{\text{SiO}_2}/N_{\text{FeNi}}$  ratio and shell thickness is summarized in **Figure 7(a)**. Notably, the shell thickness increased with an increasing  $N_{\text{SiO}_2}/N_{\text{FeNi}}$  ratio. To further understand the significance of applying different  $N_{\text{FeNi}}$ , the correlation between the  $N_{\text{FeNi}}$  and the estimated number of particles from the final product ( $N_f$ ) synthesized using various amounts of supplied  $\text{SiO}_2$  is presented (**Figure 7(b)**).  $N_f$  was estimated from the total number of FeNi cores ( $N_{\text{FeNi}}$ ) and free silica particles ( $N_{\text{free-SiO}_2}$ ) with a measured average diameter of 25 nm (**Figure S6** and the detailed explanation is elucidated in Supporting Information). In the FeNi@SiO<sub>2</sub> particle formation mechanism, the HMDSO possibly transforms to SiO<sub>2</sub> monomers, nuclei, and clusters scavenged on the FeNi core particle by deposition—that is, heterogeneous nucleation (**Figure 7 (c)**). If the FeNi core is absent, the HMDSO possibly changes to SiO<sub>2</sub> monomers, nuclei, clusters, and particles consecutively, leading to homogenous nucleation (gas-to-particle reaction). The dashed line in **Figure 7(b)** corresponds to the theoretical number of free silica nanoparticles ( $N_{\text{free-SiO}_2,\text{theo}}$ ) produced by homogeneous nucleation in the absence of an FeNi core at various amounts of the supplied SiO<sub>2</sub> monomer. Meanwhile, the black solid line, when  $N_f$  is equal to  $N_{\text{FeNi}}$ , indicates that all the supplied SiO<sub>2</sub> monomers perfectly coated the FeNi particles through heterogeneous nucleation, implying no free silica nanoparticle generation.

The comparison of the dashed line with the estimated  $N_f$  according to the experimental results (open sphere, square, and triangle) shown in **Figure 7(b)** indicated that the presence of the FeNi core suppressed homogeneous nucleation.  $N_{\text{FeNi}}$  affects the suppression of homogeneous nucleation toward heterogeneous nucleation. Specifically, high  $N_{\text{FeNi}}$  can lead to heterogeneous nucleation more effectively than low  $N_{\text{FeNi}}$  because low  $N_{\text{FeNi}}$  can limit the mixing between supplied SiO<sub>2</sub> and FeNi among the gas flow in the reactor as well as the available surface area for

SiO<sub>2</sub> deposition. In addition, low  $N_{\text{FeNi}}$  led to a high SiO<sub>2</sub> concentration that may have caused the gas-to-particle reaction (homogeneous nucleation). When this reaction occurs, the large cluster might generate and scavenge on one side of the FeNi core particle due to coagulation from the Van der Waals motion, leading to inhomogeneous shell thickness (**Figure 7 (c)**). The plausibility of this mechanism is intricately supported by the use of a high amount of supplied HMDSO and preheater temperature, resulting in the rapid SiO<sub>2</sub> monomer generation. Hence, this increases the SiO<sub>2</sub> monomer concentration surrounding the FeNi particles. To provide further insight into the variation of  $N_{\text{FeNi}}$  during the coating process, **Figure S7** is included in the Supporting Information. Notably, a high  $N_{\text{FeNi}}$  in FeNi@SiO<sub>2</sub> particle synthesis is crucial for providing the particles with good coating characteristics. This observation is in good agreement with previous studies related to chemical vapor deposition.<sup>32,33,38,40</sup>

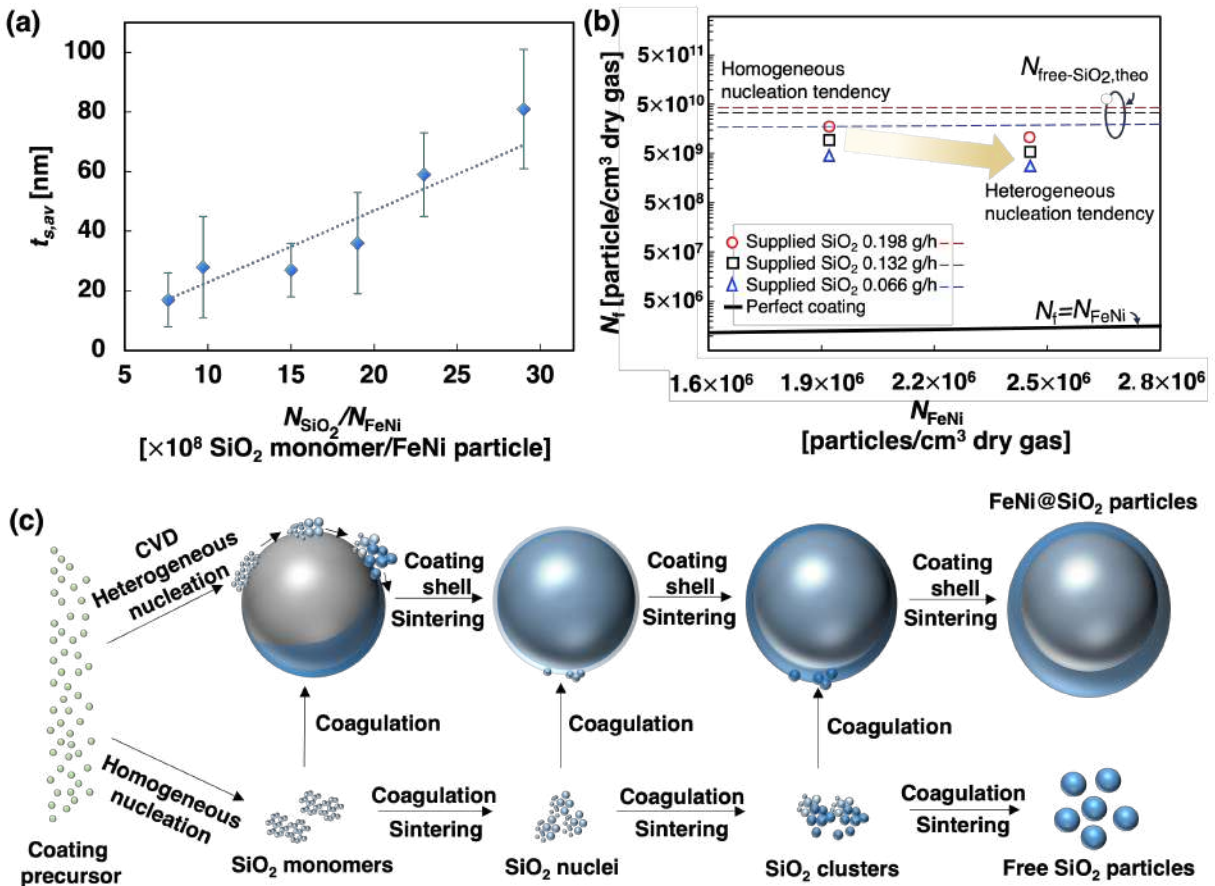


**Figure 7.** (a) Effect of the  $N_{\text{SiO}_2}/N_{\text{FeNi}}$  ratio on shell thickness, (b) estimated number of particles from the final product ( $N_f$ ) to the total number of FeNi cores ( $N_{\text{FeNi}}$ ) in different amounts of supplied  $\text{SiO}_2$ , and (c) schematic image of the plausible  $\text{FeNi}@\text{SiO}_2$  particle formation.

### 3.3. Significance of coating characteristics on powder core properties

To comprehensively probe the impact of shell thickness and coating characteristics on core loss properties,  $\text{FeNi}@\text{SiO}_2$  particles with low shell inhomogeneity were also applied to powder cores. **Figure 8(a)** presents the eddy current loss and packing density characteristics of the powder cores after applying **FNS-2.5-3.8** ( $t_{\text{s,ave}}$  5 nm, shell inhomogeneity 27%) and **FNS-2.5-7.6** ( $t_{\text{s,ave}}$  17 nm, shell inhomogeneity 29%) samples. Notably, at the same level of normalized eddy current loss, the **FNS-2.5-7.6** samples yielded a higher packing density, hovering around 82%, relative to the **FNS-2.5-3.8** samples (approximately 81%). The samples had markedly different normalized eddy current loss values at lower packing densities. For instance, at a packing density of 80%, the **FNS-2.5-3.8** sample had a normalized eddy current loss of 0.78, markedly exceeding that of **FNS-2.5-7.6** (measuring approximately 0.5) (see **Figure 8(b)**). These results suggest that  $\text{FeNi}@\text{SiO}_2$  particles with thicker silica shells contribute to reduced eddy current losses, potentially due to increased resistance to eddy current flow resulting from the thicker silica shell, which is a nonconductive material.<sup>51–53</sup> This behavior is limited when the shell inhomogeneity is low. In contrast, unexpected outcomes were observed in the **FNS-2.5-23** and **FNS-1.9-29** samples, as the normalized eddy current loss increased with increasing shell thickness and shell inhomogeneity, characterized by average shell thicknesses ( $t_{\text{s,ave}}$ ) of 53 nm and 80 nm and shell inhomogeneities of 53% and 79%, respectively. The substantial values of normalized eddy current loss from powder



cores prepared using FeNi@SiO<sub>2</sub> particles with high shell inhomogeneity underscore the importance of this factor. Higher shell inhomogeneity not only intensifies the discrepancy between  $t_{s,thin}$  and  $t_{s,thick}$  shells but also exposes some FeNi cores (see **Figure 6**), potentially localizing eddy current losses in areas with very thin or uncoated shells. These findings represent an initial step toward understanding the relationship between the shell thickness of secondary particles and the eddy current loss of powder cores, paving the way for further comprehensive investigations in real-world applications.

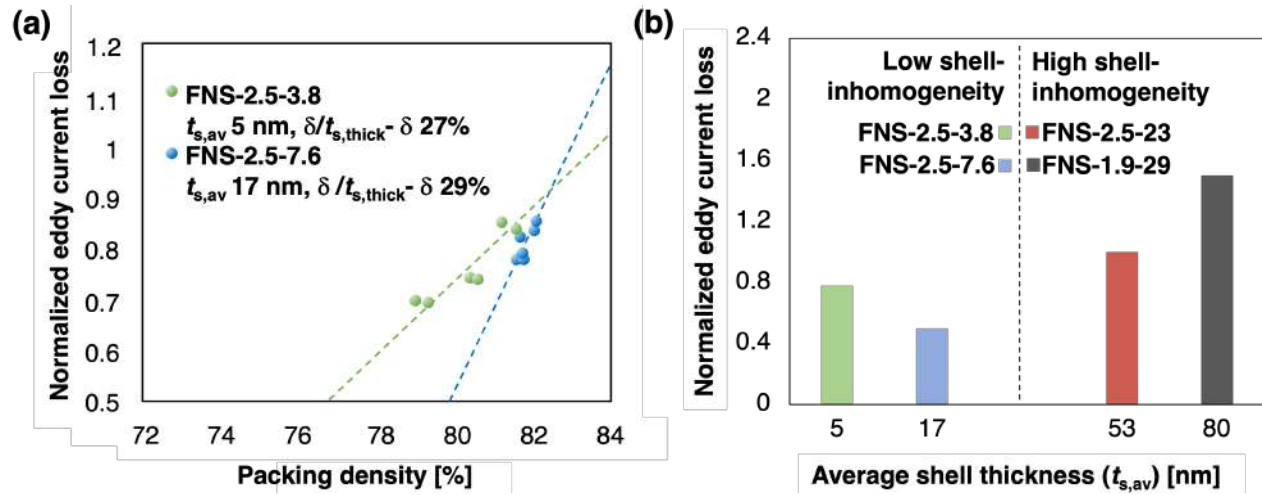


**Figure 8.** (a) Normalized eddy current loss in various packing densities of powder cores comprising FeNi@SiO<sub>2</sub> particles from FNS-2.5-3.8 and FNS-2.5-7.6 as secondary particles. (b) Correlation of the average shell thickness and normalized eddy current loss from various samples with different shell inhomogeneities.

The importance of shell inhomogeneity was also observed in the normalized breakdown voltage from the powder core prepared using samples of FNS-2.5-7.6 and FNS-1.9-29 (see **Figure 9(a)**). The sample with  $t_{s,ave}$  of 80 nm and shell inhomogeneity of 79% (FNS-1.9-29) provided a normalized breakdown voltage of around 0.3 at a packing density of 80%. This value was 10 times lower than that of the sample with  $t_{s,ave}$  of 17 nm and shell inhomogeneity of 29% (FNS-2.5-7.6). **Figure 9 (b)** illustrates the plausible mechanism of the eddy current loss generation through the

uncoated, uniformly coated, and non-uniformly coated particles. In the case of uncoated particles, the inter- and intra-particle eddy current occurs. In contrast, uniformly coated particles can suppress the inter-particle eddy current. However, when the shell thickness is lacking homogeneity, uneven electric current flow causes localized eddy current loss between particles due to exposed FeNi particles or very thin shell thickness, causing partially inter-particle eddy current occurs. This is similar to breakdown voltage. Exposed FeNi particles or those with thin shells on one side may have lower breakdown voltages because the electric field can easily cause current leakage and breakdown across these exposed or thinly insulated particles. This investigation further emphasizes the significance of shell inhomogeneity when applying FeNi@SiO<sub>2</sub> particles to powder cores. This investigation further emphasizes the significance of shell inhomogeneity when applying FeNi@SiO<sub>2</sub> particles to powder cores.

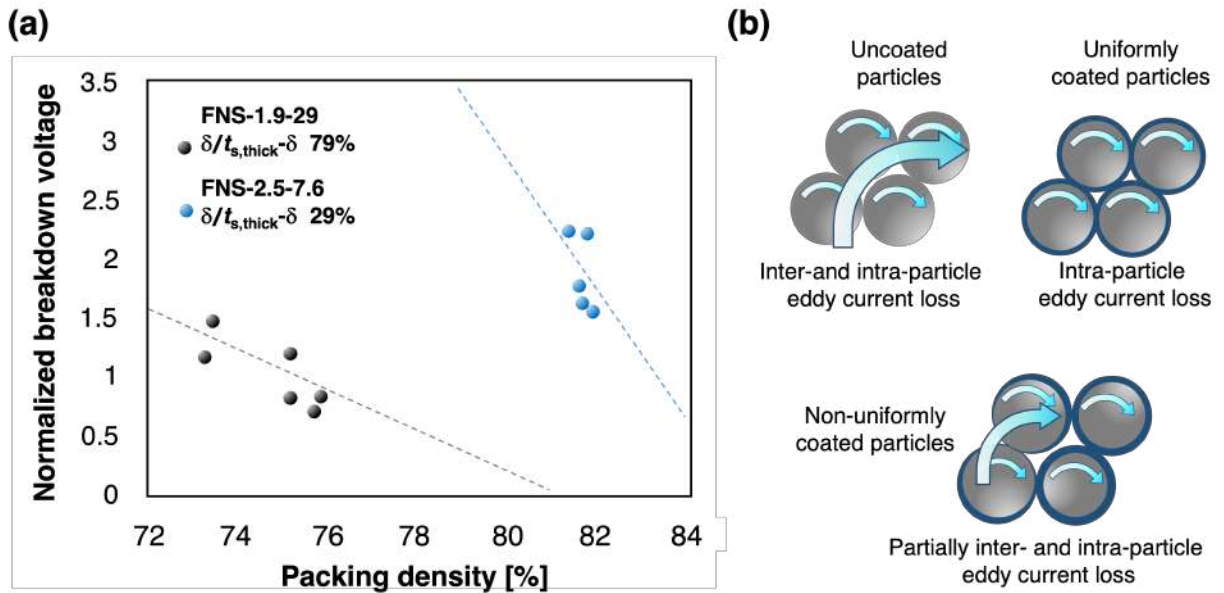


**Figure 9.** (a) Normalized breakdown voltage at various packing densities of powder cores comprising FeNi@SiO<sub>2</sub> particles from **FNS-2.5-7.6** and **FNS-1.9-29** as secondary particles. (b) Schematic image of the eddy current loss through uncoated, uniformly coated, non-uniformly coated particles.



#### 4. Conclusions

Nanostructured FeNi@SiO<sub>2</sub> particles with different coating characteristics were synthesized by aerosol method via swirler-assisted spray pyrolysis. Different numbers of FeNi core particles ( $N_{\text{FeNi}}$ ) with concentrations of  $1.9 \times 10^6$  and  $2.5 \times 10^6$  FeNi particle/cm<sup>3</sup> dry gas, denoted as **FNS-1.9-29** and **FNS-2.5-23**, were supplied to the system. The particle characteristics of both samples revealed significant differences in nanoscale shell thickness, shell inhomogeneity, and the presence of silica nanoparticles. **FNS-1.9-29** showed a thicker average nano-scaled shell thickness, higher percentage of shell inhomogeneity, and a notable amount of free silica nanoparticles. When incorporated into a powder core, it exhibited higher eddy current loss and lower breakdown voltage than **FNS-2.5-23**. This result was attributed to the higher shell inhomogeneity and the larger quantity of silica nanoparticle impurities in **FNS-1.9-29**. Furthermore, to understand the coating process phenomena at nanoscale, the supplied amount of silica monomer (0.4 nm) was varied, leading to different ratios of silica monomers to FeNi core particles. This study uncovered that controlling  $N_{\text{FeNi}}$  is critical for obtaining nanostructured FeNi@SiO<sub>2</sub> particles with satisfactory coating characteristics. In addition, a comparative analysis of particles with varying shell thicknesses and inhomogeneity levels further emphasized that maintaining uniform shell thickness (low shell inhomogeneity) across the particles is crucial for optimal powder core properties. These findings underscore the importance of meticulous control over coating characteristics during nanostructuring process to achieve superior powder core properties. In the future work, it is imperative to advance synthesis methodologies by integrating online measurement systems, such as particle size distribution analyzers. This integration facilitates real-time monitoring and

adjustment of relevant parameters in a feedback loop control process. This approach ensures high-quality particle production and advances the development of innovative materials.

## **ASSOCIATED CONTENT**

### **Supporting Information**

The supporting information is provided including the experimental set-up for calculating the number of FeNi precursor droplet, the theoretical amount of supplied silica, the morphology of FeNi particles, the normalized permeability of the FeNi@SiO<sub>2</sub> particles, the TEM image and shell thickness distribution of **FNS-2.5-3.8**, the calculation of free silica particles, and effect of the  $N_{\text{FeNi}}$  during the coating process. (PDF)

## **AUTHOR INFORMATION**

### **Corresponding Author**

Takashi Ogi – Email: [ogit@hiroshima-u.ac.jp](mailto:ogit@hiroshima-u.ac.jp). Tel: +81-82-424-3765

### **ORCID**

Takashi Ogi: 0000-0003-3982-857X  
Eka Lutfi Septiani: 0000-0002-9845-2376  
Kiet Le Anh Cao: 0000-0001-9986-6127  
Tomoyuki Hirano: 0000-0003-3622-0606

### **Author Contributions**

The manuscript was written through contributions of all authors. All authors have given approval to the final version of the manuscript.

## Note

The authors declare no competing financial interest.

## Acknowledgements

This work was supported by JSPS KAKENHI Grant Number JP23H01745. This work is partly supported by the International Network on Polyoxometalate Science at Hiroshima University, the JSPS Core-to-Core Program, the Information Center of Particle Technology, Japan, and the Hosokawa Powder Technology Foundation. We would like to thank the Ministry of Education, Culture, Sports, Science and Technology (MEXT) of Japan for providing a doctoral scholarship to E. L. S. We thank Dr. Makoto Maeda of the Natural Science Center for Basic Research and Development (N-BARD) at Hiroshima University for TEM observations and discussion.

## References

- (1) Hirano, T.; Tsuboi, T.; Ho, T. T. N.; Tanabe, E.; Takano, A.; Kataoka, M.; Ogi, T. Porosity Engineering of Pt-Loaded Nb-SnO<sub>2</sub> Catalyst Layers in Polymer Electrolyte Fuel Cells. *ACS Appl Energy Mater* **2023**.
- (2) Le, P. H.; Kitamoto, Y.; Yamashita, S.; Cao, K. L. A.; Hirano, T.; Amen, T. W. M.; Tsunoji, N.; Ogi, T. Macropore-Size Engineering toward Enhancing the Catalytic Performance of CO Oxidation over Three-Way Catalyst Particles. *ACS Appl Mater Interfaces* **2023**, *15* (46), 54073–54084.

- (3) Nguyen, T. T.; Saipul Bahri, N. S. N.; Rahmatika, A. M.; Cao, K. L. A.; Hirano, T.; Ogi, T. Rapid Indomethacin Release from Porous Pectin Particles as a Colon-Targeted Drug Delivery System. *ACS Appl Bio Mater* **2023**, 6 (7), 2725–2737.
- (4) Cao, K. L. A.; Kito, Y.; Le, P. H.; Ogi, T.; Hirano, T. Synthesis of Spherical  $\beta$ -Quartz Solid-Solution Particles Derived from Cordierite Using a Flame Process. *ACS Applied Engineering Materials* **2023**, 1 (7), 1789–1798.
- (5) Bahri, N. S. N. S.; Nguyen, T. T.; Hirano, T.; Matsumoto, K.; Watanabe, M.; Morita, Y.; Ogi, T. Enhancing Water Stability of Nanostructured Cellulose Nanofiber Particle through the Application of Oxazoline Cross-Linker. *Advanced Powder Technology* **2023**, 34 (12).
- (6) Rahmatika, A. M.; Yuan, W.; Arif, A. F.; Balgis, R.; Miyajima, K.; Anilkumar, G. M.; Okuyama, K.; Ogi, T. Energy-Efficient Templating Method for the Industrial Production of Porous Carbon Particles by a Spray Pyrolysis Process Using Poly(Methyl Methacrylate). *Ind Eng Chem Res* **2018**, 57 (33), 11335–11341.
- (7) Gutfleisch, O.; Willard, M. A.; Brück, E.; Chen, C. H.; Sankar, S. G.; Liu, J. P. Magnetic Materials and Devices for the 21<sup>st</sup> Century: Stronger, Lighter, and More Energy Efficient. *Advanced Materials*. February 15, 2011, pp 821–842.
- (8) Knott, A.; Andersen, T. M.; Kamby, P.; Pedersen, J. A.; Madsen, M. P.; Kovacevic, M.; Andersen, M. A. E. Evolution of Very High Frequency Power Supplies. *IEEE J Emerg Sel Top Power Electron* **2014**, 2 (3), 386–394.
- (9) Yan, Y.; Moss, J.; Ngo, K. D. T.; Mei, Y.; Lu, G. Q. Additive Manufacturing of Toroid Inductor for Power Electronics Applications. *IEEE Trans Ind Appl* **2017**, 53 (6), 5709–5714.
- (10) Septiani, E. L.; Kikkawa, J.; Cao, K. L. A.; Hirano, T.; Okuda, N.; Matsumoto, H.; Enokido, Y.; Ogi, T. DC Bias Characteristic Enhancement of the Powder Core by Using Densified

- Submicron Sized FeNi Particles through Spray Pyrolysis. *J Mater Chem C Mater* **2022**, *10* (21), 8288–8295.
- (11) Shokrollahi, H.; Janghorban, K. Soft Magnetic Composite Materials (SMCs). *J Mater Process Technol* **2007**, *189* (1–3), 1–12.
  - (12) Lotfi, A. W.; Wilkowski, M. A. Issues and Advances in High-Frequency Magnetics for Switching Power Supplies. *Proceeding of the IEEE* **2001**, *89* (6), 833–845.
  - (13) Silveyra, J. M.; Ferrara, E.; Huber, D. L.; Monson, T. C. Soft Magnetic Materials for a Sustainable and Electrified World. *Science*. American Association for the Advancement of Science October 26, 2018.
  - (14) Ammar, M.; Mazaleyrat, F.; Bonnet, J. P.; Audebert, P.; Brosseau, A.; Wang, G.; Champion, Y. Synthesis and Characterization of Core-Shell Structure Silica-Coated Fe<sub>29.5</sub>Ni<sub>70.5</sub> Nanoparticles. *Nanotechnology* **2007**, *18* (28).
  - (15) Septiani, E. L.; Yamashita, S.; Cao, K. L. A.; Hirano, T.; Okuda, N.; Matsumoto, H.; Enokido, Y.; Ogi, T. One-Step Aerosol Synthesis of SiO<sub>2</sub>-Coated FeNi Particles by Using Swirler Connector-Assisted Spray Pyrolysis. *Ind Eng Chem Res* **2022**, *61* (49), 17885–17893.
  - (16) Zhao, Y.; Ni, C.; Kruczynski, D.; Zhang, X.; Xiao, J. Q. Exchange-Coupled Soft Magnetic FeNi-SiO<sub>2</sub> Nanocomposite. *Journal of Physical Chemistry B* **2004**, *108* (12), 3691–3693.
  - (17) Septiani, E. L.; Yamashita, S.; Ratnasari, D.; Cao, K. L. A.; Hirano, T.; Okuda, N.; Matsumoto, H.; Widiyastuti, W.; Ogi, T. Enhancing Soft Magnetic Characteristics of Dense Submicron FeNi Particles with Low Carbon Content by Swirler Connector Assisted Spray Pyrolysis. *Chem Eng Sci* **2024**, 288.

- (18) Kazimierczuk, M. K. *High-Frequency Magnetic Components*, Second edition.; John Wiley & Sons Ltd: Chichester, 2014, 39-40.
- (19) Kitamoto, Y.; Cao, K. L. A.; Le, P. H.; Abdillah, O. B.; Iskandar, F.; Ogi, T. A Sustainable Approach for Preparing Porous Carbon Spheres Derived from Kraft Lignin and Sodium Hydroxide as Highly Packed Thin Film Electrode Materials. *Langmuir* **2022**, 38 (11), 3540–3552.
- (20) Wu, S.; Dong, Y.; Zhao, R.; Li, X.; Wu, H.; Gao, W.; He, A.; Li, J.; Liu, X. Microstructure Evolution and Soft Magnetic Property Optimization of Core-Shell FeSiBCCr@SiO<sub>2</sub>&ZrO<sub>2</sub> Amorphous Magnetic Powder Cores. *Ceram Int* **2023**, 49 (5), 7515–7523.
- (21) Teleki, A.; Suter, M.; Kidambi, P. R.; Nelson, B. J.; Pratsinis, S. E. Hermetically Coated Superparamagnetic Fe<sub>2</sub>O<sub>3</sub> Particles with SiO<sub>2</sub> Nanofilms. *Chem. Mater.* **2009**, 21, 10, 2094–2100.
- (22) Post, P.; Wurlitzer, L.; Maus-Friedrichs, W.; Weber, A. P. Characterization and Applications of Nanoparticles Modified In-Flight with Silica or Silica-Organic Coatings. *Nanomaterials* **2018**, 8 (7), 1–19.
- (23) Jiang, H. Y.; Zhong, W.; Wu, X. L.; Tang, N. J.; Liu, W.; Du, Y. W. Direct and Alternating Current Magnetic Properties of FeNi Particles Coated with SiO<sub>2</sub>. *J Alloys Compd* **2004**, 384 (1–2), 264–267.
- (24) Buesser, B.; Pratsinis, S. E. Design of Aerosol Coating Reactors: Precursor Injection. *Ind Eng Chem Res* **2011**, 50 (24), 13831–13839.
- (25) Nandiyanto, A. B. D.; Akane, Y.; Ogi, T.; Okuyama, K. Mesopore-Free Hollow Silica Particles with Controllable Diameter and Shell Thickness via Additive-Free Synthesis. *Langmuir* **2012**, 28 (23), 8616–8624.

- (26) Balgis, R.; Sago, S.; Anilkumar, G. M.; Ogi, T.; Okuyama, K. Self-Organized Macroporous Carbon Structure Derived from Phenolic Resin via Spray Pyrolysis for High-Performance Electrocatalyst. *ACS Appl Mater Interfaces* **2013**, 5 (22), 11944–11950.
- (27) Ogi, T.; Fukazawa, H.; Rahmatika, A. M.; Hirano, T.; Cao, K. L. A.; Iskandar, F. Improving the Crystallinity and Purity of Monodisperse Ag Fine Particles by Heating Colloidal Sprays In-Flight. *Ind Eng Chem Res* **2020**, 59 (13), 5745–5751.
- (28) Nakakura, S.; Ogi, T. Hexagonal Cesium Tungsten Bronze Nanoparticles Produced by Solvent-Free Spray Pyrolysis and Their near Infrared Absorption Properties. *J Mater Chem C Mater* **2021**, 9 (25), 8037–8042.
- (29) Chung, S. T.; Tu, Y. H.; Huang, H. Y.; Hu, C. C.; Tsai, D. H. Aerosol Synthesis of Vanadium Oxide-Carbon Hybrid Nanoparticle Clusters for High-Performance Lithium Extraction via Electrochemical Deionization. *ACS Sustain Chem Eng* **2022**, 10 (48), 15777–15790.
- (30) Buesser, B.; Pratsinis, S. E. Design of Aerosol Particle Coating: Thickness, Texture and Efficiency. *Chem Eng Sci* **2010**, 65 (20), 5471–5481.
- (31) Jain, S.; Fotou, G. P.; Kodas, T. T. A Theoretical Study on Gas-Phase Coating of Aerosol Particles. *J Colloid Interface Sci* **1997**, 185 (1), 26–38.
- (32) Okuyama, K.; Ushio, R.; Kousaka, Y.; Flagan, R. C.; Seinfeld, J. H. Particle Generation in a Chemical Vapor Deposition Process with Seed Particles. *AIChE Journal* **1990**, 36 (3), 409–419.
- (33) Boies, A. M.; Roberts, J. T.; Girshick, S. L.; Zhang, B.; Nakamura, T.; Mochizuki, A. SiO<sub>2</sub> Coating of Silver Nanoparticles by Photoinduced Chemical Vapor Deposition. *Nanotechnology* **2009**, 20 (29).

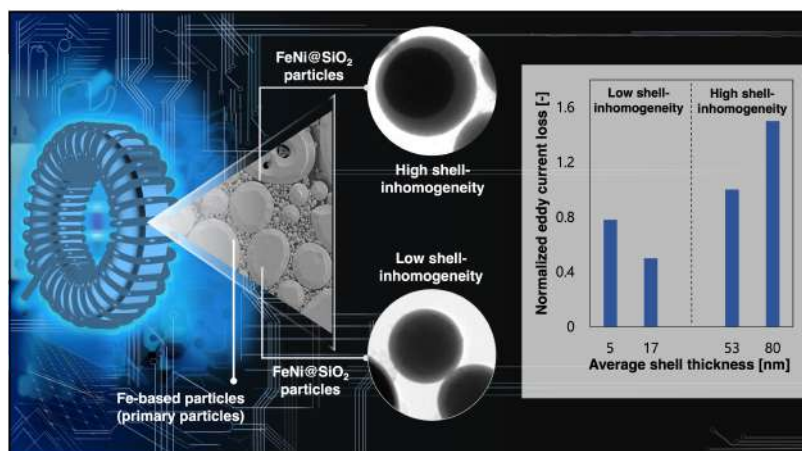
- (34) Powell, Quint H., George P. Fotou, Toivo T. Kodas, Bruce M. Anderson, and Y. Guo. Gas-Phase Coating of TiO<sub>2</sub> with SiO<sub>2</sub> in a Continuous Flow Hot-Wall Aerosol Reactor. *Materials Research* **1997**, 12 (2), 552-559.
- (35) Dasgupta, M.; Fortugno, P.; Wiggers, H. Plasma-Assisted Gas-Phase Synthesis and in-Line Coating of Silicon Nanoparticles. *Plasma Processes and Polymers* **2020**, 17 (5).
- (36) Post, P.; Jidenko, N.; Weber, A. P.; Borra, J. P. Post-Plasma SiO<sub>x</sub> Coatings of Metal and Metal Oxide Nanoparticles for Enhanced Thermal Stability and Tunable Photoactivity Applications. *Nanomaterials* **2016**, 6 (5).
- (37) Nomoev, A. V.; Bardakhanov, S. P.; Schreiber, M.; Bazarova, D. G.; Romanov, N. A.; Baldanov, B. B.; Radnaev, B. R.; Syzrantsev, V. V. Structure and Mechanism of the Formation of Core-Shell Nanoparticles Obtained through a One-Step Gas-Phase Synthesis by Electron Beam Evaporation. *Beilstein Journal of Nanotechnology* **2015**, 6 (1), 874–880.
- (38) Teleki, A.; Buesser, B.; Heine, M. C.; Krumeich, F.; Akhtar, M. K.; Pratsinis, S. E. Role of Gas - Aerosol Mixing during in Situ Coating of Flame-Made Titania Particles. *Ind Eng Chem Res* **2009**, 48 (1), 85–92.
- (39) Sotiriou, G. A.; Hirt, A. M.; Lozach, P.; Teleki, A.; Krumeich, F.; Pratsinis, S. E. Hybrid , Silica-Coated , Janus-Like Plasmonic-Magnetic Nanoparticles. **2011**, 1985–1992.
- (40) Buesser, B.; Pratsinis, S. E. Design of Gas-Phase Synthesis of Core-Shell Particles by Computational Fluid-Aerosol Dynamics. *AIChE Journal* **2011**, 57 (11), 3132–3142.
- (41) Ratnasari, D.; Septiani, E. L.; Cao, K. L. A.; Hirano, T.; Okuda, N.; Matsumoto, H.; Ogi, T. Synthesis of Submicron-Sized Spherical Silica-Coated Iron Nickel Particles with Adjustable Shell Thickness via Swirler Connector-Assisted Spray Pyrolysis. *Langmuir* **2023**, 39 (39), 14063–14073.



- (42) Septiani, E. L.; Kikkawa, J.; Cao, K. L. A.; Hirano, T.; Okuda, N.; Matsumoto, H.; Enokido, Y.; Ogi, T. Direct Synthesis of Submicron FeNi Particles via Spray Pyrolysis Using Various Reduction Agents. *Advanced Powder Technology* **2021**, 32 (11), 4263–4272.
- (43) Saravanan, P.; Jose, T. A.; Thomas, J.; Kulkarni, G. U. Submicron Particles of Co, Ni and Co-Ni Alloys. *Bull. Mater. Sci* **2001**, 24 (5), 515–521.
- (44) Xia, B.; Lenggoro, I. W.; Okuyama, K. Preparation of Nickel Powders by Spray Pyrolysis of Nickel Formate. *Journal of the American Ceramic Society* **2001**, 84 (7), 1425–1432.
- (45) Chi, Q.; Chang, L.; Dong, Y.; Zhang, Y.; Zhou, B.; Zhang, C.; Pan, Y.; Li, Q.; Li, J.; He, A.; Wang, X. Enhanced High Frequency Properties of FeSiBPC Amorphous Soft Magnetic Powder Cores with Novel Insulating Layer. *Advanced Powder Technology* **2021**, 32 (5), 1602–1610.
- (46) Ulrich, G. D. Theory of Particle Formation and Growth in Oxide Synthesis Flames. *Combustion Science and Technology* **1971**, 4 (1), 47–57.
- (47) Tsantilis, S.; Pratsinis, S. E. Soft- and Hard-Agglomerate Aerosols Made at High Temperatures. *Langmuir* **2004**, 20 (14), 5933–5939.
- (48) Zhang, W.; Qu, L.; Pei, H.; Qin, Z.; Didier, J.; Wu, Z.; Bobe, F.; Ingber, D. E.; Weitz, D. A. Controllable Fabrication of Inhomogeneous Microcapsules for Triggered Release by Osmotic Pressure. *Small* **2019**, 15 (42).
- (49) Kollár, P.; Birčáková, Z.; Füzer, J.; Bureš, R.; Fáberová, M. Power Loss Separation in Fe-Based Composite Materials. *J Magn Magn Mater* **2013**, 327, 146–150.
- (50) Keizou Ohta. *Fundamental of Magnetic Engineering II*; Kyoritsu Zensho, 1973, 310 (*In Japanese*).

- (51) Du, Y.; Liu, W.; Qiang, R.; Wang, Y.; Han, X.; Ma, J.; Xu, P. Shell Thickness-Dependent Microwave Absorption of Core-Shell Fe<sub>3</sub>O<sub>4</sub>@C Composites. *ACS Appl Mater Interfaces* **2014**, *6* (15), 12997–13006.
- (52) Luo, F.; Fan, X.; Luo, Z.; Hu, W.; Li, G.; Li, Y.; Liu, X.; Wang, J. Ultra-Low Inter-Particle Eddy Current Loss of Fe<sub>3</sub>Si/Al<sub>2</sub>O<sub>3</sub> Soft Magnetic Composites Evolved from FeSiAl/Fe<sub>3</sub>O<sub>4</sub> Core-Shell Particles. *J Magn Magn Mater* **2019**, *484*, 218–224.
- (53) Wang, Z.; Bi, H.; Wang, P.; Wang, M.; Liu, Z.; Shen, L.; Liu, X. Magnetic and Microwave Absorption Properties of Self-Assemblies Composed of Core-Shell Cobalt-Cobalt Oxide Nanocrystals. *Physical Chemistry Chemical Physics* **2015**, *17* (5), 3796–3801.

## Table of Content (TOC) graphic



## Supporting Information:

# Effects of Coating Characteristics of One-Step Aerosol Synthesized–Silica-Coated FeNi Nanostructured Particles on Powder Core Properties for Electronic Machines Development

*Eka Lutfi Septiani <sup>a</sup>, Nobuhiro Okuda <sup>b</sup>, Hiroyuki Matsumoto <sup>b</sup>, Kiet Le Anh Cao <sup>a</sup>,  
Tomoyuki Hirano <sup>a</sup>, and Takashi Ogi <sup>a \*</sup>*

<sup>a</sup>Chemical Engineering Program, Department of Advanced Science and Engineering,  
Graduate School of Advanced Science and Engineering, Hiroshima University, 1-4-1  
Kagamiyama, Higashi-Hiroshima, Hiroshima 739-8527, Japan

<sup>b</sup>Materials Research Center, Technology & Intellectual Property HQ, TDK corporation,  
570-2 Matsugashita, Minami-Hadori, Narita, Chiba 286-8588, Japan

\*Corresponding author: Takashi Ogi, [ogit@hiroshima-u.ac.jp](mailto:ogit@hiroshima-u.ac.jp)

Tel/Fax: +81-82-424-3765

## **Table of contents**

- 1. Experimental set-up for calculating the number of FeNi precursor droplet.**
- 2. Theoretical amount of supplied silica.**
- 3. The morphology of FeNi particles.**
- 4. Silica shell thickness characteristics.**
- 5. Normalized permeability of the FeNi@SiO<sub>2</sub> particles.**
- 6. The characteristics of FNS-2.5-3.8 sample.**
- 7. Calculation of free silica particles.**
- 8. Effect of the  $N_{\text{FeNi}}$  during the coating process.**

## 1. Experimental setup for calculating the number of FeNi precursor droplets

To predict the number of supplied FeNi particles, it was assumed to be the same as the number of FeNi precursor droplets. The experimental setup for calculating the number of droplets is shown in **Figure S1**. The precursor concentration, consisting of  $\text{Fe}(\text{NO}_3)_3 \cdot 9\text{H}_2\text{O}$  and  $\text{Ni}(\text{NO}_3)_2 \cdot 6\text{H}_2\text{O}$  in 25 vol% ethanol/water, was 0.2 mol/L. The precursor solution was transferred to a nebulizer using a peristaltic pump with volumetric liquid feed rates of 0.8 and 1.0 mL/min. The FeNi precursor was subsequently nebulized by the ultrasonic NE-U78 nebulizer to generate precursor droplets, which served as feed into the system. The generated droplets were carried at a carrier gas flow rate into a countercurrent condenser at 6°C. In the condenser, the droplets were condensed and captured in a flat-bottom flask surrounded by an ice bath at -1°C. In this study, the rate of atomization of the precursor volume ( $Q_p$ ) was calculated by measuring the change in precursor volume using Equation (S1):

$$Q_p = \frac{V_{\text{atomized}}}{t} = \frac{V_o - V_r - V_n}{t} \quad (\text{S1})$$

where  $V_o$  is the original volume of liquid (ml), which is measured from the as-prepared precursor to be transported into the nebulizer.  $V_r(t)$  is the remaining volume of liquid from the original volume (ml), which is measured from the remaining precursor after 30 min ( $t$ ) of observation.  $V_n(t)$  is the remaining volume of liquid in the nebulizer cup (mL) after 30 min of observation. Afterward, the number of droplets ( $N_{\text{FeNi}}$ ) was expressed in terms of the total carrier gas ( $Q_g$ ) calculated from Equation (S2).

$$N_{\text{FeNi}} = \frac{Q_p}{V_d Q_g} \quad (\text{S2})$$

where  $V_d$  is the volume of the droplet generated by the ultrasonic nebulizer, which is assumed to be a sphere with an average diameter of 4.6  $\mu\text{m}$  based on the ultrasonic nebulizer specification.  $Q_g$  is the total gas fed into the reactor, which is FeNi precursor carrier gas ( $Q_c$ ), additional gas ( $Q_a$ ), and HMDSO carrier gas ( $Q_s$ ).

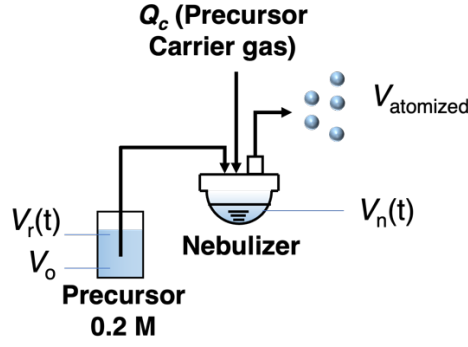


**Figure S1.** Experimental setup for calculating the number of FeNi precursor droplets.

## 2. Theoretical amount of the supplied silica

The amount of supplied silica carried by the HMDSO carrier gas ( $Q_s$ ) was calculated theoretically based on the HMDSO vapor pressure ( $P_{\text{HMDSO}}^v$ ) using the Antoine Equation at a temperature of  $8^\circ\text{C}$  ( $T_s$ ), as described in Equation (S2). The constant properties of HMDSO (A, B, and C) follow CAS No. 107-46-0.

$$\log_{10} P_{\text{HMDSO}}^v = A - \frac{B}{T_s + C} \quad (\text{S2})$$

The fraction of HMDSO ( $x_{\text{HMDSO}}$ ) and the volumetric rate of supplied HMDSO ( $Q_{\text{HMDSO}}$ ) were then predicted using Equations (S3) and (S4), respectively. Furthermore, by assuming an ideal gas condition, the mole of HMDSO was calculated using Equation (S5).

$$x_{\text{HMDSO}} = \frac{P_{\text{HMDSO}}^v}{P} \quad (\text{S3})$$

$$x_{\text{HMDSO}} = \frac{Q_{\text{HMDSO}}}{Q_{\text{HMDSO}} + Q_s} \quad (\text{S4})$$

$$PQ_{\text{HMDSO}} = n_{\text{HMDSO}}RT_s \quad (\text{S5})$$

where  $P$  is the total pressure from the HMDSO carrier gas ( $Q_s$ ),  $n_{\text{HMDSO}}$  is molar rate of the supplied HMDSO, and  $R$  is the ideal gas constant. Then, the generated silica ( $n_{\text{SiO}_2}$ ) was estimated twice of  $n_{\text{HMDSO}}$  so that the mass rate of the supplied silica ( $m_{\text{SiO}_2}$ ) could be calculated by multiplying by the molecular weight of the silica. Adjusting the  $Q_s$  to 10, 20, and 30 mL/min yielded the  $m_{\text{SiO}_2}$  of 0.066, 0.132, and 0.198 g/h, respectively. Eventually, the

volumetric rate of supplied silica ( $V_{\text{SiO}_2}$ ) was predicted by dividing the  $m_{\text{SiO}_2}$  by the silica density ( $\rho_{\text{SiO}_2}$ ), resulting in 0.03, 0.06, and 0.09 cm<sup>3</sup>/h, respectively. The amount of supplied silica was calculated based on the smallest silica monomer that could possibly exist. In this study, a diameter of 0.4 nm was assumed, represented as two tiniest silica molecules from the reaction of HMDSO to silica.

### 3. The morphology of FeNi particles

The successful synthesis of FeNi@SiO<sub>2</sub> could be indicated from the comparison of the morphology of synthesized FeNi particles alone. **Figure S2** represents the SEM and TEM images of the FeNi particles.

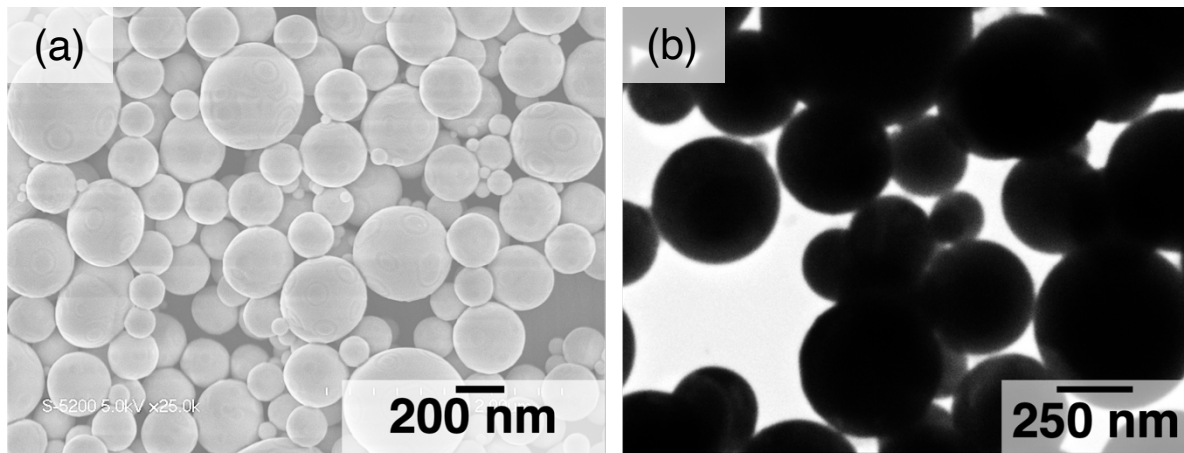


**Figure S2.** (a) SEM and (b) TEM images of the synthesized FeNi particles.

### 4. Silica shell thickness characteristics

Silica shell thickness was characterized by the average shell thickness and shell thickness inhomogeneity. The average shell thickness was calculated using Equation (S6), while the shell thickness inhomogeneity was calculated as a percentage using Equation (S7). The dimensions for the calculation were based on the TEM images represented in **Figure S3**.

$$t_{s,ave} = average \left( \sum \frac{d_{p,i} - d_{c,i}}{2} \right) \quad (S6)$$

$$\%Inhomogeneity = \frac{\delta}{t_{s,thick} - \delta} \times 100\% \quad (S7)$$



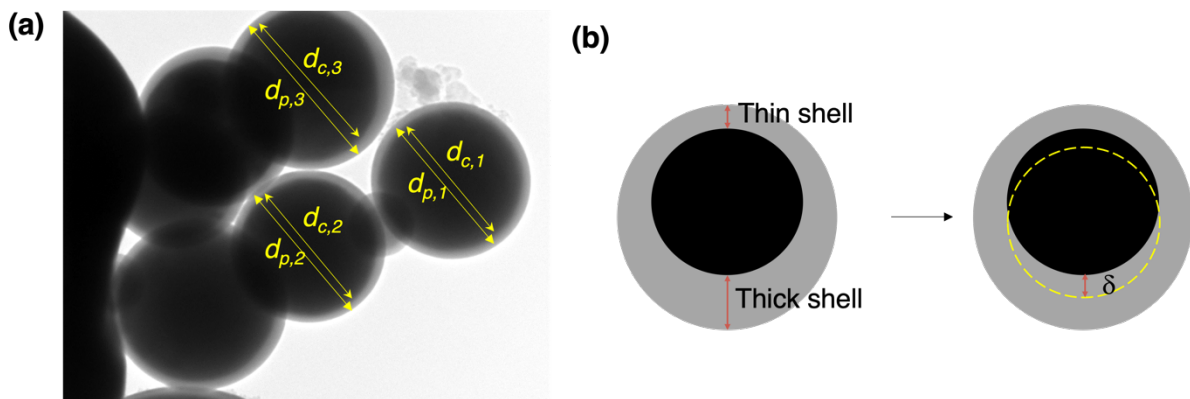


**Figure S3.** Dimensions for calculating (a) average shell thickness and (b) shell thickness inhomogeneity.

## 5. Normalized permeability of the FeNi@SiO<sub>2</sub> particles

To further understand the different coating characteristics of the FeNi@SiO<sub>2</sub> particles, the normalized permeability of some samples was observed and represented in **Figure S4**.

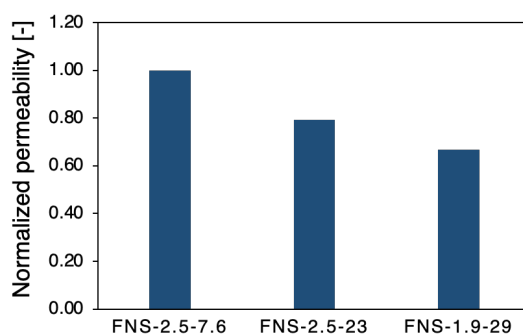


**Figure S4.** The normalized permeability of the FeNi@SiO<sub>2</sub> particles with different coating characteristics

## 6. Characteristics of the FNS-2.5-3.8 sample

To understand the trend of the effect of  $N_{\text{SiO}_2}/N_{\text{FeNi}}$  ratio on the shell thickness characteristics, **FNS-2.5-3.8** was produced.

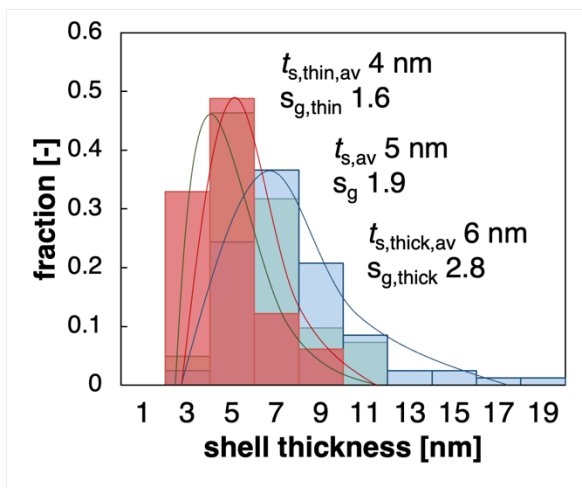
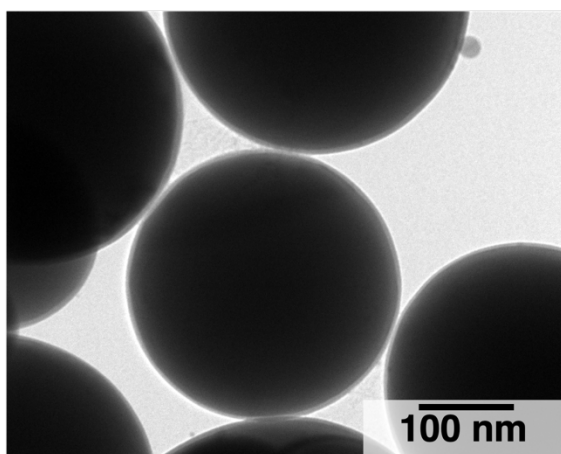


**Figure S5.** TEM image and shell thickness distribution of the FNS-2.5–3.8 sample.

## 7. Calculation of free silica particles

Silica particles were formed when homogeneous nucleation occurred. Some of the silica particles were scavenged on the FeNi core particles due to coagulation, whereas the others remained as free silica nanoparticles. The volume of free silica ( $V_{\text{freeSiO}_2}$ ) particles was estimated by calculating the volume difference between the supplied silica and the silica that coated the FeNi core particles. Accordingly, the number of free silica particles was calculated by dividing  $V_{\text{freeSiO}_2}$  by the volume of a single silica particle with a diameter of 25 nm, which was counted by measuring the silica diameter from the SEM images, as shown in **Figure S6**. This calculation was used to estimate the number of particles in the final product ( $N_f$ ).

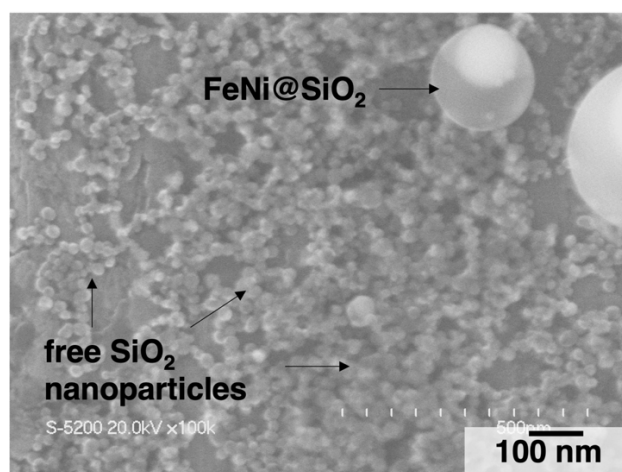


**Figure S6.** Free SiO<sub>2</sub> nanoparticles observed by SEM analysis.

## 8. Effect of the $N_{\text{FeNi}}$ during the coating process

The effect of the  $N_{\text{FeNi}}$  on the coating process can be illustrated in **Figure S7**. a high  $N_{\text{FeNi}}$  promotes heterogeneous nucleation more effectively compared to a low  $N_{\text{FeNi}}$ . This is because a high  $N_{\text{FeNi}}$  provides an even mixing between the supplied  $\text{SiO}_2$  and FeNi within the gas flow in the reactor, as well as provide a sufficient available surface area for  $\text{SiO}_2$  deposition (performing heterogeneous nucleation). In a same supply amount of  $\text{SiO}_2$  source, a low  $N_{\text{FeNi}}$  results in a relatively high  $\text{SiO}_2$  concentration, which may trigger gas-to-particle reactions (homogeneous nucleation). Moreover, the high  $\text{SiO}_2$  concentration is in the near distance from the FeNi core particles that leads to the coagulation of  $\text{SiO}_2$  on the FeNi core particle, resulting in an uneven shell thickness.

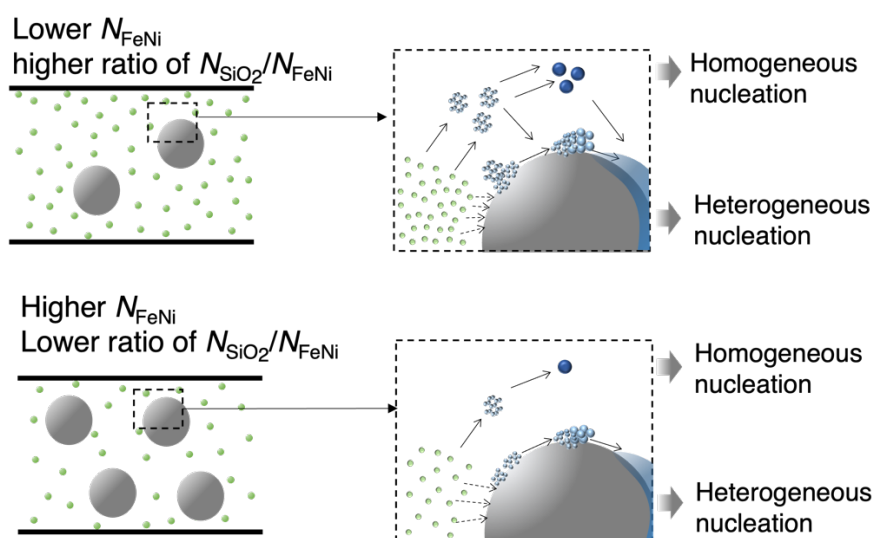


**Figure S7.** The scheme of coating process in the different  $N_{\text{FeNi}}$ .